Modeling and experimental investigation of induction welding of thermoplastic composites and comparison with other welding processes

Gouin O'Shaughnessey, Patrice; Dube, M; Fernandez Villegas, Irene

DOI
10.1177/0021998315614991

Publication date
2016

Document Version
Final published version

Published in
Journal of Composite Materials

Citation (APA)
Gouin O'Shaughnessey, P., Dube, M., & Fernandez Villegas, I. (2016). Modeling and experimental investigation of induction welding of thermoplastic composites and comparison with other welding processes. *Journal of Composite Materials*, *50*(21), 2895-2910. https://doi.org/10.1177/0021998315614991

Article

JOURNAL OF COMPOSITE MATERIALS

Journal of Composite Materials
2016, Vol. 50(21) 2895–2910

DOI: 10.1177/0021998315614991
jcm.sagepub.com
SAGE

Modeling and experimental investigation of induction welding of thermoplastic composites and comparison with other welding processes

Patrice Gouin O'Shaughnessey[1], Martine Dubé[1] and Irene Fernandez Villegas[2]

Abstract

A three-dimensional finite element model of the induction welding of carbon fiber/polyphenylene sulfide thermoplastic composites is developed. The model takes into account a stainless steel mesh heating element located at the interface of the two composite adherends to be welded. This heating element serves to localize the heating where it is needed most, i.e. at the weld interface. The magnetic, electrical, and thermal properties of the carbon fiber/polyphenylene sulfide composite and other materials are identified experimentally or estimated and implemented in the model. The model predicts the temperature–time curves during the heating of the composite and is used to define processing parameters leading to high-quality welded joints. The effect of the heating element size and input current on the thermal behavior is investigated, both experimentally and using the developed model. The welds quality is assessed through microscopic observations of the weld interfaces, mechanical testing, and observations of the fracture surfaces. A comparison with two other welding processes, namely resistance welding and ultrasonic welding is finally conducted.

Keywords

Thermoplastic composites, joint/joining, finite element analysis, welding

Introduction

Joining is inevitable in the design of large and complex composite structures. Structures made of thermosetting composites rely mainly on two joining processes: adhesive bonding and mechanical fastening. Both of these processes come with a number of disadvantages such as a high sensitivity to surface preparation and long curing times for adhesive bonding as well as delamination and stress concentrations due to holes drilling for mechanical fastening. These two joining processes can be avoided when a structure is made of thermoplastic composites. In effect, thermoplastic composites offer the possibility to be assembled by welding. Welding consists in heating a thermoplastic composite over its glass transition (amorphous polymer) or melting (semi-crystalline polymer) temperature and allowing it to cool down under the application of pressure. It is a fast process, of the order of seconds, and is not sensitive to surface preparation. The aerospace industry has already begun to use welding as an assembly method for parts made of thermoplastic composites. For example, the leading edges of the wings of the Airbus A340-600 and A380 are assembled by resistance welding (RW), and the empennage of the Gulfstream G650 is assembled by induction welding (IW).[1] Another welding process that shows potential to be used at large scale is ultrasonic welding (UW).[2]

In the RW process, an electrically conductive heating element (HE) connected to a power supply is placed

---

[1] Department of Mechanical Engineering, École de technologie supérieure, Montréal, Québec, Canada

[2] Department of Structural Integrity and Composites, Delft University of Technology, Delft, The Netherlands

Corresponding author:
Martine Dubé, Department of Mechanical Engineering, École de technologie supérieure, 1100 Notre-Dame Street West, Montréal, Québec, Canada, H3C 1K3.
Email: martine.dube@etsmtl.ca

at the interface of two thermoplastic composite parts to be welded (adherends). An electrical current is applied to the HE which heats up by Joule effect. The polymer located in the vicinity of the HE softens or melts and when the current is stopped, the assembly cools down, under the application of pressure, to form a welded joint. Carbon fiber fabrics were historically used as HE; however, in the past years, it was shown that HE in the form of stainless steel meshes of various sizes offer a better process control and a more uniform temperature over the weld area.[3] UW is a process in which low amplitude and high-frequency vibrations, in the range of kHz, are transmitted to the thermoplastic composite adherends by a sonotrode. As opposed to the RW process, heat is generated by surface and intermolecular friction which occurs due to the high-frequency vibrations. Energy directors, i.e. man-made neat polymer protrusions located at the weld interface, are used to localize the heating at the weld line. Historically, energy directors were made of rectangular or triangular shapes. Recently, Villegas[4] successfully used flat energy directors to weld thermoplastic composite adherends which facilitated the process control.

IW is based on a high-frequency alternating electrical current circulating in a coil. The coil generates a time-variable magnetic field (MF) of the same frequency as the current. If an electrical conductor is placed in the vicinity of the MF, eddy currents are induced, leading to heat generation by Joule losses. This principle is used to weld thermoplastic composites. Here again, an electrically conductive HE is placed between the two adherends. An electrical current is applied to the coil until the polymer located close to the HE softens or melts. The current is then stopped, allowing the polymer to cool down under the application of pressure. Similarly to the RW process, the HE remains trapped in the weld after the welding operation. The HE may consist in a stainless steel mesh of various dimensions or a magnetic susceptor. Alternatively, if the adherends are made of carbon fiber fabric, no HE is necessary as the fiber architecture allows for current close loops to exist. These loops may be sufficient to generate heat without having to add any foreign material to the weld stack. However, in such a case, heat would be concentrated at the surface of the top adherend, i.e. the adherend located closest to the coil. Heat then propagates through the thickness of the adherend until it reaches the location where it is needed, i.e. the weld interface. A way of cooling the top adherend, or preventing it from overheating, is needed in order to avoid deformation of the coupon or structure.[5] Induction heating of unidirectional (UD) carbon fiber adherends is less effective than for fabric-based adherends, even for quasi-isotropic or cross-ply lay-ups. Adding a HE element at the weld interface of two UD fiber-based adherends helps generate and concentrate the heat at the weld interface. With the development of new manufacturing methods such as automated fiber placement, UD fiber reinforcement is more and more popular. UD reinforcement also provides the composite with high strength and stiffness, making these materials ideal candidates for many aerospace applications. As Bayerl et al.[6] and Ahmed et al.[7] reported, very few studies have focused on thermoplastic composites IW based on a HE. Therefore, a study on welding of UD carbon fiber thermoplastic composites with an HE is needed and relevant. Furthermore, although such an HE is a foreign material that one may want to avoid, it was shown in studies on RW that it does not affect the weld mechanical performance in a negative way. Even under fatigue loading, good mechanical performance was reported for joints made by RW with a stainless steel mesh HE.[8]

The first numerical works about induction heating of composites were dedicated to the identification of the dominant heating mechanisms. Many authors claimed that Joule heating within the carbon fibers is mainly responsible for the temperature increase,[9–19] while others[20–23] believed that heating occurs at the fiber junctions. This last heating mechanism relies on dielectric heating or Joule losses caused by contact resistance at fiber junctions. Yarlagadda et al.[22] developed a model that identified the dominant heating mechanism as a function of the dielectric junction impedance, fiber resistivity, and contact resistance. In all cases, losses at junctions were dominant over fiber heating unless the contact resistance between the fibers was very low. On the other side, Mitschang et al.[11] demonstrated that carbon fiber with or without resin heated up equally, meaning that dielectric heating would be less important than fiber Joule heating and contact resistance at junctions. It is interesting to mention that the methodology for the measurement of the electrical resistance of the adherend proposed by Rudolf et al.,[24] which was also used by Mitschang et al.,[11] takes into account both the fiber resistance *and* the junction resistance. Thus, by using such a measurement as an input value, fiber Joule losses and junction Joule losses were implicitly included in the models. Finally, it should be noted that the heating mechanism depends on several parameters such as the material type (consolidated or non-consolidated plies), fiber architecture (fabric or UD) and lay-up, matrix, and induction heating process parameters like the frequency.[22] Furthermore, the heating mechanism can evolve during heating as the matrix softens and allows for a better contact between the fibers.[12,22]

Recent work on the simulation of the IW process is summarized in Table 1. Results from Duhovic et al.[13,14,16] showed the heating of a carbon fiber/

Table 1. Overview of induction heating modeling studies.

Reference	Results	Notes
Mitschang et al.[11]	The model predicted the temperature measured by an infrared camera on a laminate (fabric).	The comparison was limited to a heating time of 4 s and temperature of 160 °C. The electrical resistivity of the laminates was not provided.
Moser[12]	The model predicted the temperature measured by a pyrometer on a laminate (fabric).	The electrical resistivity of the composite was temperature-independent. The heating time was 14 s corresponding to a laminate temperature of 400 °C.
Duhovic et al.[13]	The predicted temperature was overestimated due to the constant electrical resistivity of the composite (fabric).	The prediction agreed with experimental data up to 15 s of heating and then overshooted.
Bensaid et al.[17,18]	The model predicted the temperature of a laminate made of UD carbon fiber.	The maximum predicted temperature was 110 °C. The electrical resistivity of the composite was temperature-independent.
Wasselynck et al.[19]	The model considered the heating of each individual ply.	The maximum predicted temperature was 110 °C, and overshooting of the prediction was beginning at this temperature due to constant electrical resistivity of the fiber.

UD: unidirectional.

poly-ether-ether-ketone composite plate located 2 mm away from a coil up to a temperature of around 250 °C. The simulation consisted in a three-dimensional (3D) multiphysics finite element model (FEM) but did not consider an HE nor magnetic flux concentrators which are known to increase the MF intensity.[6] Most authors attempted to predict the temperature of a composite laminate rather than a joint, and they all considered a temperature-independent carbon fiber electrical resistivity. As Duhovic et al.[13,14] mentioned, a constant carbon fiber electrical resistivity leads to a temperature overestimation. Finally, the majority of the models were not compared to experimental data at high temperatures, i.e. passed the polymer melting point or after a long heating time.

The present study has two objectives and main contributions. The first objective is the development of a numerical model capable of predicting the temperature increase of composite adherends welded by induction, using a stainless steel HE and a magnetic flux concentrator. To the authors' best knowledge, such a numerical model predicting the heating of two UD carbon fiber thermoplastic composite adherends to be welded by induction, including the experimental setup, the effect of a stainless steel mesh, and magnetic flux concentrator, does not exist. In addition, and contrarily to what is available in the literature, the model takes into account the temperature dependency of material properties such as the electrical conductivity and heat capacity. In order to build the model, experimental identification or estimation of various material properties was carried out. Welding experiments were also conducted in order to validate the predictions of the model. The second objective and contribution is an understanding of the effects of the HE size on the heating of composite adherends by induction and the resulting joints mechanical performance. Although previous studies were conducted on the optimization of the HE size for the RW process,[3] IW may lead to different conclusions as the heating mechanism is different from that of RW. The eddy currents will be more or less effective depending upon the mesh size.

A comparative study is finally conducted to confirm results published recently on welding of carbon fiber/polyphenylene sulfide (CF/PPS) twill weave fabric as to the advantages and disadvantages of the three welding processes described above.[2] Since the material used here is UD CF/PPS composites, the comparison with IW involves an HE at the weld interface, as opposed to what was published previously.

Experimental

Materials and specimen geometry

Thermoplastic composite laminates were compression-molded from UD pre-impregnated plies of CF/PPS material (AS4/TC110 from Ten Cate Advanced Composite USA Inc.). Sixteen plies were stacked in a quasi-isotropic lay-up $[(0/90/\pm45)_2]_s$ for a thickness of 2.12 mm. The laminates were manufactured as per Ten Cate recommendations, i.e. processing temperature of 320 °C, holding time of 20 min, and molding pressure of 0.7 MPa. The average cooling rate was 21 °C/min. The coupons were cut off using a water-cooled diamond saw to dimensions of 101.6 mm × 25.4 mm and welded in a lap shear configuration as per the ASTM D1002 standard (Figure 1).

Induction welding

The IW setup included an induction heating device (power supply and work head), a pneumatic cylinder to apply pressure, a welding jig, and a temperature acquisition system. The induction heating device was a 10 kW Ambrell Easy Heat machine with a frequency ranging from 150 kHz to 450 kHz and maximum output current of 750 A. The power supply automatically selected an optimal current frequency of 268 kHz, based on the material to be heated and the coil's impedance. This frequency was selected so that it maximizes the coupling between the coil and HE. The hairpin type coil, shown on Figure 2(a), was made of a square section copper tube of 6.35 mm side. The specimens were located under the coil and away from the connection with the work head so that the MF disturbances close to the connection did not affect the heating of the specimens (Figure 2(a)).

The HE (Figure 2(b)) consisted of stainless steel meshes of four various sizes as presented in Table 2. One neat PPS resin film (thickness of 0.07 mm) was placed on each side of the HE in order to have a resin-rich zone at the weld interface. As shown on Figure 2(c), ceramic blocks were used to apply pressure without affecting the MF. A magnetic flux concentrator was integrated to the setup in order to increase the MF intensity. Thanks to their high magnetic permeability, magnetic flux concentrators are known to reduce processing times in induction heating and welding of various materials.[25] The location of the magnetic flux concentrator is shown on Figure 2(c). Placing it on top of the coil helped concentrating the coil's current density on the bottom of the cross-section, as illustrated in Figure 3. The magnetic flux concentrator width was selected based on preliminary experiments. A width of 22.6 mm was deemed good enough to reduce the edge effect on the short edge on the joint (Figure 1) and improve the temperature homogeneity.

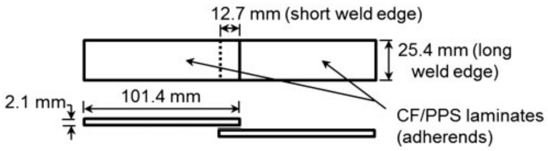

Figure 1. Lap shear specimen geometry.
CF/PPS: carbon fiber/polyphenylene sulfide.

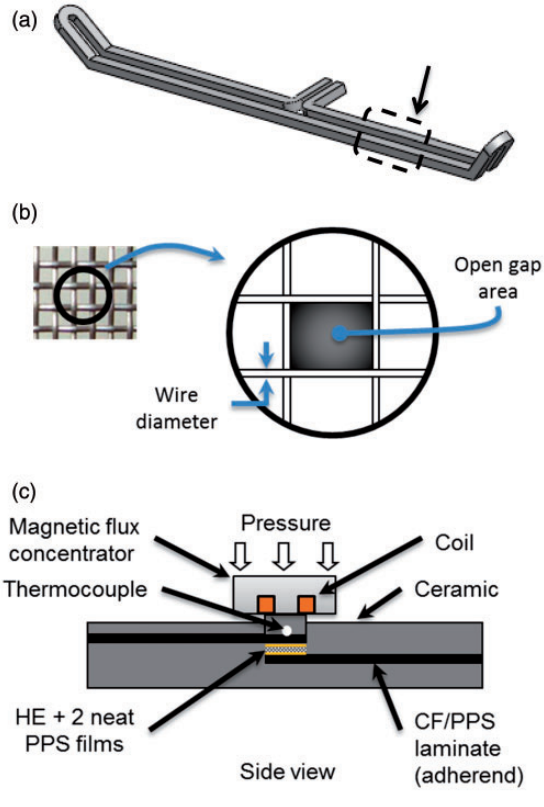

Figure 2. (a) Coil geometry, (b) heating element geometry, and (c) schematic of the induction welding setup.
CF/PPS: carbon fiber/polyphenylene sulfide; HE: heating element.

Table 2. Heating element characteristics, taking into account the neat PPS resin films.[30,32,33]

Parameters/properties	HE A	HE B	HE C	HE D
Wire density (nb of wires/25.4 mm)	150	200	325	400
Wire diameter (mm)	0.06	0.04	0.03	0.02
Fraction of open area (%)	37.4	47.0	42.0	44.0
Density (kg/m^3)	2 769	2 191	2 128	1 914
Specific heat (J/(kg°C))	653	715	724	758
k_x, k_y (W/(mK))	1.79	1.16	1.07	0.83
k_z (W/(mK))	0.51	0.33	0.29	0.26
σ_{xy} at 293 K (S/m)	138 378	83 811	75 611	55 331
σ_{xy} at 400 K (S/m)	123 639	74 884	67 557	49 437
σ_{xy} at 700 K (S/m)	99 459	60 239	54 345	39 769
σ_z (S/m)	10			
μ_r	1			

See Figure 7 for the *x*, *y*, and *z* directions.
PPS: polyphenylene sulfide; HE: heating element.

The temperature was monitored using a thermocouple sandwiched between the ceramic block insulator and the upper adherend (Figure 2(c)). The input current in the coil was turned off when the thermocouple's temperature reached 260 °C. This temperature was selected experimentally so that the temperature at the weld interface reached the PPS welding temperature of 320 °C everywhere over the weld area. A pressure of 0.5 MPa was applied during welding.[26] Four input currents and four HE geometries were used, for a total of 13 IW configurations (Table 3). The input current values were selected so that the minimum and maximum welding times were 30 s and 90 s, respectively. In effect, welding times shorter than 30 s would not allow for a complete weld to be achieved and would lead to poor lap shear strengths (LSS). A complete weld is achieved when the weld interface reaches the polymer melting temperature everywhere but does not reach the polymer degradation temperature anywhere.[7,9] On the other hand, welding times longer than 90 s would promote deformation of the adherends.

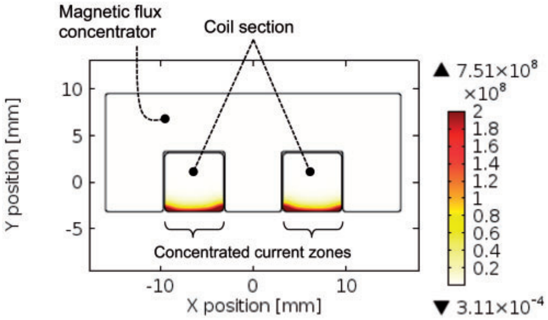

Figure 3. Effect of the magnetic flux concentrator on the current density (A/m^2), as obtained from simulations run with the help of Comsol. The current density is concentrated at the bottom of the coil's cross-section, as a result of the magnetic flux concentrator being located on top of the coil.

Resistance welding

The RW setup included a power supply (maximum output current and voltage of 45 A and 70 V,

Table 3. Welding parameters for various configurations.

Induction welding

Configuration	Heating element	Input current (A)	Number of welded specimens
1	A	450	3
2	A	500	3
3	A	525	3
4	A	550	3
5	B	500	3
6	B	525	3
7	B	550	3
8	C	500	3
9	C	525	10
10	C	550	3
11	D	500	3
12	D	525	3
13	D	550	3

Resistance welding

Configuration	Heating element	Input power (W/m^2)	Number of welded specimens
14	B	130,000	3

Ultrasonic welding

Configuration	Peak to peak amplitude (μm)	Pressure (MPa)	Energy (J)	Time (s)	Number of welded specimens
15	84	1.25	670	0.48	3

respectively), a computer control and data acquisition system, and a welding jig (Figure 4). The input power to be applied to the HE was selected so that a welding time of 55 s was achieved. A pressure of 0.5 MPa was applied during welding. The clamping distance, defined as the distance between the copper electrical connectors and the edge of the adherends, was 0.5 mm (Figure 4). It corresponds to the portion of the HE that is exposed to air. Air cooling was applied on the sides of the welds to avoid overheating of the edges.[27] Only the HE B was used (Table 2) based on previous work from Dubé et al.[3] on the RW process. This HE was shown to be the one leading to the highest mechanical performance in resistance-welded joints. As for IW, PPS films of a thickness of 0.07 mm were added above and below the HE.

Ultrasonic welding

UW was done with a Rinco Dynamic 3000 machine which can deliver up to 3000 W at 20 kHz. A rectangular sonotrode was used. The specimen clamping and alignment was ensured by a jig described in Villegas et al.[2] Flat energy directors consolidated in a hot platen press out of four neat PPS films (total thickness of 0.4 mm) were located at the weld interface (Figure 5). The welding parameters were chosen based on Villegas[4] and are summarized in Table 3.

Mechanical testing and characterization methods

Lap shear tests were conducted in a servo-hydraulic MTS testing machine according to the ASTM D1002 standard. The machine was operated under displacement control at a crosshead speed of 1.3 mm/min. All tests were conducted under ambient environmental conditions. The mechanical tests were stopped when complete failure of the specimens occurred. The LSS was calculated by dividing the maximum tensile force registered during the test by the overlap area. Proper flow of the polymer across the weld interface was verified through observations of the specimen's cross-section by optical microscopy. Ten specimens were induction-welded according to configuration #9 in Table 3 in order to verify the repeatability of the process. The mechanical performance of these specimens was consistent with an average LSS of 28.8 MPa and a standard deviation of 0.7 MPa. Since a good repeatability was obtained, only three specimens were welded for each other welding configuration.

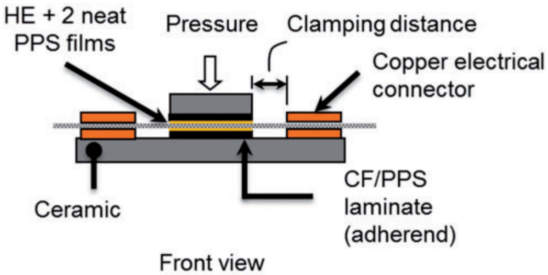

Figure 4. Schematic of the resistance welding setup. CF/PPS: carbon fiber/polyphenylene sulfide; HE: heating element.

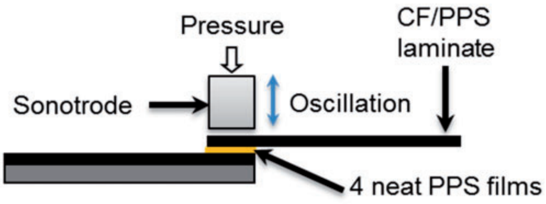

Figure 5. Schematic of the ultrasonic spot welding setup. CF/PPS: carbon fiber/polyphenylene sulfide.

Finite element modeling of IW

The simulation of the IW process was conducted with the help of the finite element Comsol Multiphysics® software, which is well-known for its multiphysics capability and has a pre-assembled induction heating module. A full 3D model was developed, coupling the theories of electromagnetism and heat transfer (HT). Electromagnetism equations were solved for the prediction of the eddy currents distribution in the HE and adherends. A transient HT thermal analysis then served to calculate the heat generated by the eddy currents (Joule effect) as well as the temperature distribution in the HE and adherends, as a function of time.

The induced current density is not uniform over the cross-section of the HE. In effect, the eddy currents are more important on the top surface of the HE than on the inside of it. This effect is called the "skin effect" and is characterized by the penetration depth, δ, which corresponds to the depth, measured from the surface, at which the current density is 37% of that at the surface[28]:

$$\vec{J_d} = \vec{J_0} e^{-d/\delta} \tag{1}$$

with:

$\vec{J_d}$ = Current density at a distance d from the surface of the HE (A/m^2)
$\vec{J_0}$ = Current density at the surface of the HE (A/m^2)

The penetration depth can be estimated from[28]:

$$\delta = \sqrt{\frac{\rho_e}{\pi f \mu}} \tag{2}$$

with:

ρ_e = Electrical resistivity (Ω·m)
f = Frequency of the input current (Hz)
μ = Magnetic permeability (H/m)

For example, the penetration depth of the stainless steel material is 0.82 mm, and the current density at this distance from the surface of the material is 37% of $\overrightarrow{J_0}$. Since the thickness of all the HE used in this study is thinner than the penetration depth, eddy currents cancelation occurs resulting in reduced Joule losses.[28] Therefore, thinner HE will be subjected to reduced eddy currents and heat generation compared to the thicker ones.

Materials properties

The electrical and thermal properties of many materials must be identified to correctly simulate the IW process. The composite adherends and stainless steel mesh were modeled as homogenous materials. The equivalent thermal conductivity of the composite adherends was calculated based on Holmes and Gillespie.[29] In this approach, a transformation matrix is multiplied by the conductivity matrix in order to get the thermal conductivity of a ply as a function of its orientation. The equivalent thermal conductivity of the whole adherend is then calculated. The equivalent thermal and electrical conductivities of the stainless steel mesh were calculated based on Jun and Wirtz.[30] The resulting properties are shown in Table 2 and take into account the two neat PPS films located on top and bottom of the HE.

The electrical conductivity of the adherends was measured using a setup similar to that of Rudolf et al.[24] A four wires Ohms measurement was carried out. A range of electrical conductivities was observed, and variations were obtained from one adherend to another adherend. This variation could be explained by the poor and variable contact between the fibers of two adjacent composite plies, which is affected by the composite manufacturing process, among other things. Nevertheless, the possible variation in the electrical conductivity from one adherend to another was disregarded, and a temperature-variable electrical conductivity (Figure 6) was implemented in the model and was kept the same for every simulations. The electrical conductivity values are within the range of the experimentally measured data and follow the recommendations of Duhovic et al.[13] to consider the temperature dependency of this property. They are also consistent with the properties used in Duhovic et al.[13]

The adherends' heat capacity was measured by differential scanning calorimetry and was also considered to be temperature-dependant, meaning that the latent heat of fusion was accounted for (Figure 6). All the material properties are indicated in Figure 6 and Table 2 and Table 4.

Assumptions

The assumptions made in the model are listed here:

- Adherends have a reduced length of 50 mm in order to reduce computing time.
- The thermal expansion of all materials is neglected.
- The control volume depth is 40 mm (Figure 7, x-axis).
- The coil temperature is fixed to 20 °C.
- A convection coefficient $h = 5$ W/(m^{2}K) is considered.[27,29]
- Joule losses are the only heating mechanism. However, the material electrical properties take into account the global electrical resistance of the adherends and HE. Thus, electrical resistance of fibers *and* fibers junctions are considered.

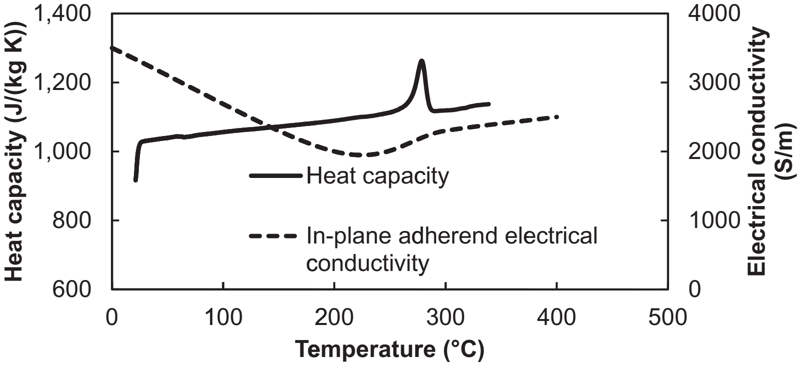

Figure 6. Heat capacity and electrical conductivity of the adherends (CF/PPS), as a function of temperature. The heat capacity was measured by DSC and the electrical conductivity was measured experimentally at room temperature and estimated for high temperatures.[13,31]
CF/PPS: carbon fiber/polyphenylene sulfide; DSC: differential scanning calorimetry.

Table 4. Materials properties used in the FEM (data measured experimentally or estimated from Holmes and Gillespie[29,33–36]).

Material properties	CF/PPS adherends (fiber volume fraction = 0.59)	Copper (coil)	MFC	Ceramic
Density (kg/m^3)	1560	8700	1000	2750
Specific heat (J/(kg°C))	See Figure 6	385	1000	1000
k_x, k_y (W/(mK))	2.22	400	4	1.26
k_z (W/(mK))	0.335	400	4	1.26
σ_x,σ_y (S/m)	See Figure 6	$5.998 \cdot 10^7$	10	10
σ_z (S/m)	10	$5.998 \cdot 10^7$	10	10
μ_r	1	1	$16/(4\pi \cdot 10^{-7})$	1

FEM: finite element model; CF/PPS: carbon fiber/polyphenylene sulfide; MFC: Magnetic Flux Concentrator.

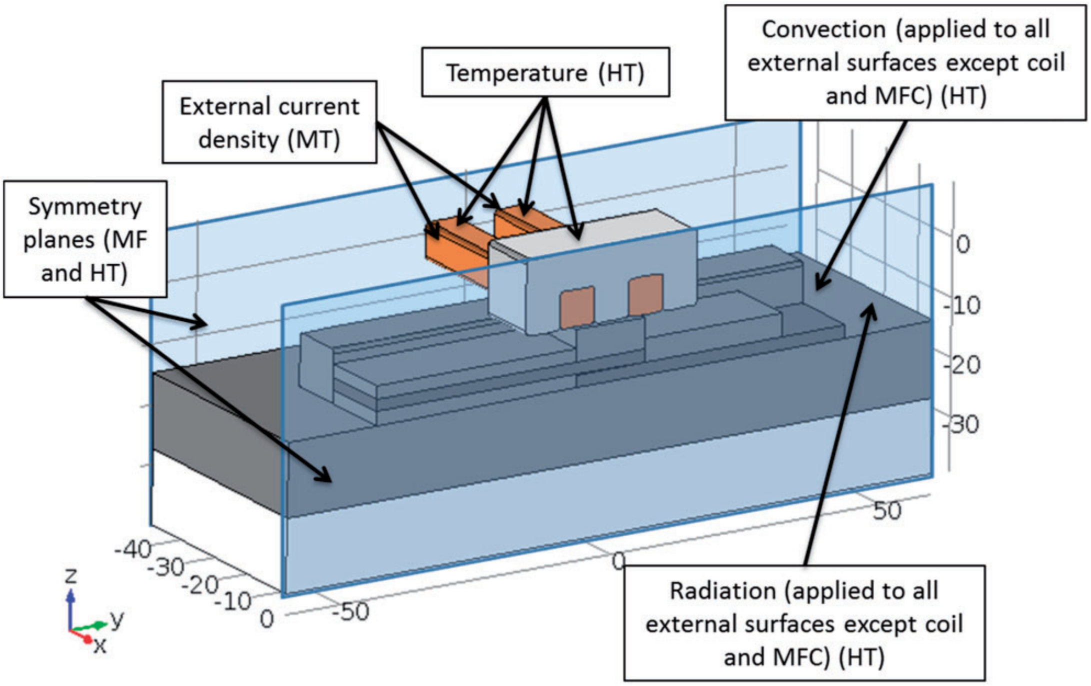

Figure 7. Induction welding FEM geometry with applied loadings and boundary conditions. MF refers to the Comsol magnetic field module and HT to the heat transfer module. Dimensions in mm.
MF: magnetic field; HT: heat transfer; FEM: finite element model; MFC: Magnetic Flux Concentrator.

- The electrical conductivity of highly resistive materials was set to 10 S/m for convergence ease.

Model definition

All geometry domains, including the surrounding air, were meshed with tetrahedral solid elements. A convergence study was conducted to get accurate results within reasonable computing time. The model took 22 h to run on a 32-GB Ram desktop computer. This simulation time was partly due to the temperature-dependant materials properties. Figure 7 shows the boundary conditions applied to domains and surfaces. One half of the joint geometry was modeled, and symmetry conditions were applied on the *yz* plane. The modeling methodology is described here and illustrated in Figure 8:

(I) The geometry is created.
(II) The material properties are input.
(III) The MF module is used to generate the MF and eddy currents. External current density is applied to the coil. Magnetic insulation is applied as a

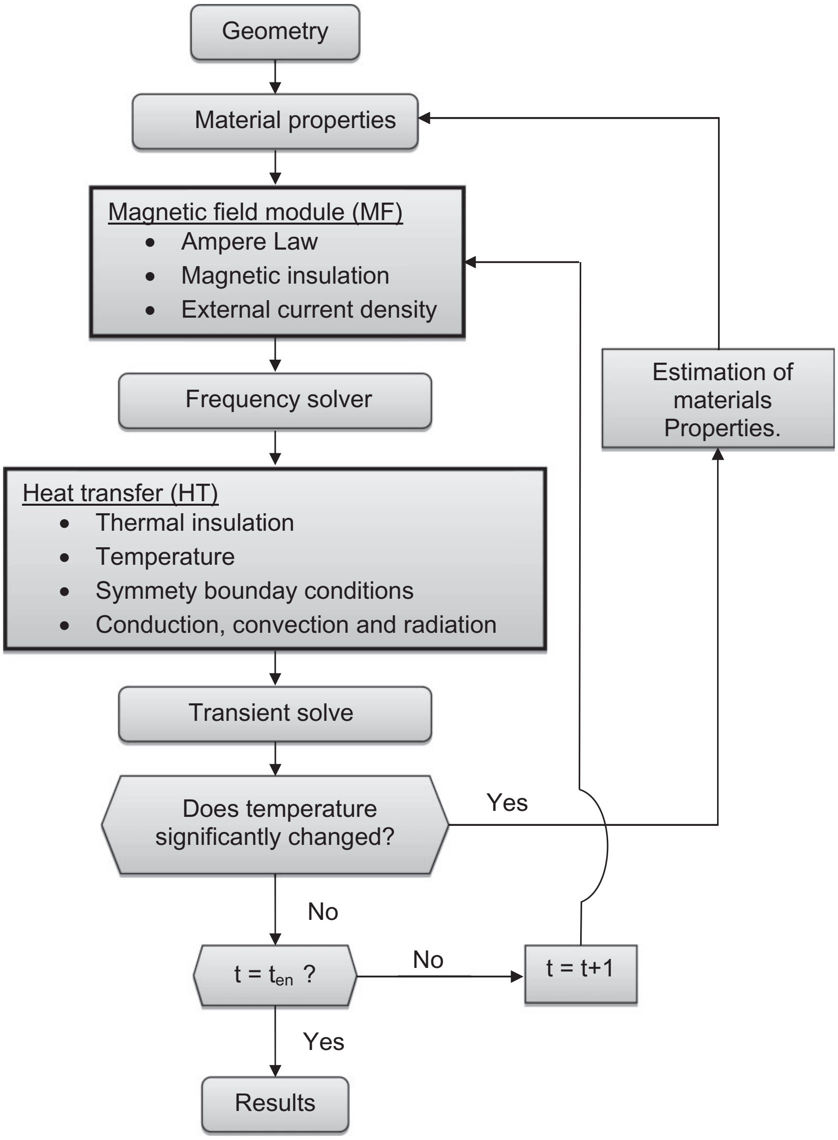

Figure 8. Modeling methodology.

boundary condition to represent the symmetry at $x = 0$ and $x = -40$ mm (see Figure 7).

(IV) HT calculations are conducted, taking into account conduction, convection, and radiation HT mechanisms.

(V) If the temperature change is larger than a pre-defined threshold, the various temperature-dependant properties of the materials are redefined, and a new calculation loop is performed. An assessment of the temperature-dependant properties of the materials is conducted with a relative tolerance of 1%, i.e. for a given result, if the recalculated properties deviate by more than 1%, a new calculation loop is performed.

(VI) When the desired heating time is reached, the model results are generated and extracted.

Induction welding

Heating behavior

The average measured heating rate at the interface between the upper adherend and the ceramic block insulator is indicated on Figure 9, for each IW configuration. The average heating rates are calculated based on the total heating time, i.e. from the time at which the current is switched on until it is turned off. The heating rate increases from HE D to HE A, for a same input current. This behavior was expected as the induced power is inversely proportional to the electrical resistance of the HE. Since HE A has the highest conductivity, i.e. the lowest resistance, it is the one providing the fastest heating rate. Moreover, the penetration depth (equation

(2)) calculated for the stainless steel material is 0.82 mm. This depth is larger than the wire diameter for all HE. In this regime, less power is induced for smaller wire diameters.[28] As Ahmed et al.[31] reported, too small a wire diameter results in a slow or insufficient heating rate. Figure 9 also shows, as expected, the increase of the heating rate with the input current in the coil.

In Figure 10, experimental and FEM temperature–time curves are compared for two different HE sizes and same input current (a) and for the same HE heated with two different input currents (b). The selected curves correspond to four different welding configurations, but it should be noted that all other configurations from Table 3 provided similar trends. The heating rate, as measured experimentally, increases after a certain heating time. This heating time corresponds to the time required for the PPS to lose important viscosity, as demonstrated experimentally by the resin flowing out of the joint. It is believed that when the PPS resin flows, the fibers of the adherends move around and come into closer contact with each other, thus increasing the electrical conductivity of the composite. This higher electrical conductivity leads to an increasing heating rate, despite the effects of cooling by conduction, convection, and radiation which are also more important at high temperatures. This phenomenon of a higher electrical conductivity once the PPS becomes less and less viscous was implemented in the model by means of a non-linear relationship between the electrical conductivity and the temperature (Figure 6). The model was used to predict the average heating rate for eight different welding configurations. The results are summarized in Table 5. Good agreement between the predicted and measured heating rates is obtained in all cases, except for one configuration involving HE A. The FEM predictions therefore provide reliable data for most cases and can be

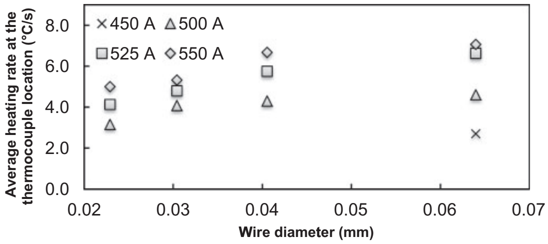

Figure 9. Average heating rate as a function of the HE wire diameter, as measured experimentally.
HE: heating element.

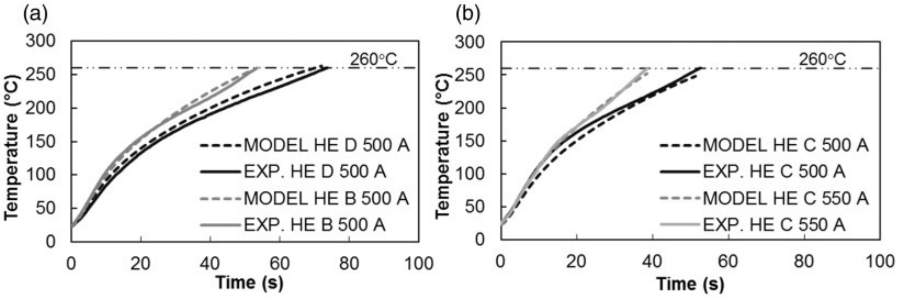

Figure 10. Temperature–time curves at the thermocouple location predicted numerically and measured experimentally for (a) IW configurations 5 and 11 and (b) IW configurations 8 and 10 (see Table 3 for the detail of the welding configurations).
HE: heating element; IW: induction welding.

Table 5. Comparison between experimental and predicted heating rates for induction-welded joints.

Induction welding configuration (see Table 3)	Experimental average heating rate (°C/s)	Predicted average heating rate (°C/s)	Error (%)
2	4.6	5.8	27%
4	7.1	8.0	13%
5	4.3	4.5	4%
7	6.7	6.3	–7%
8	4.1	4.4	7%
10	5.3	6.0	12%
11	3.2	3.3	4%
13	5.0	4.9	–1%

successfully used to define processing windows, i.e. adjusting the input current and HE size to achieve high-quality welds in a reasonable time.

The thermal maps obtained by FEM are compared to the fracture surfaces of welded specimens in Figure 11. Figure 11(a) shows the results obtained from the FEM presented previously, and Figure 11(b) shows the results of a previous investigation on RW.[27] The temperature distribution is quite different from one welding process to another. In IW, overheating is observed on the long edges of the weld (Figure 1). This "edge effect" is due to the particular location of the HE and adherends underneath the coil, which generates a higher current density on the long edges. Cold spots are also seen in every corner of the weld area. These cold spots are also visible on the fracture surfaces (Figure 11(a), right) where the resin is not completely melted in the corners. The thermal map predicted by FEM overall matches that of the welded specimens. In RW Figure 11(b), the hot zone location is changed to the short edges of the weld. Therefore, both processes have issues related to the edge effect. In IW, the edge effect is mostly due to the current density which varies over the weld area. In RW, it is generated solely by HT mechanisms and can be addressed by changing the clamping distance.[27]

Mechanical performance

The LSS of the induction-welded joints are presented on Figure 12 as a function of the average heating rate. The results present the average LSS obtained for all specimens of a same welding configuration (Table 3). In all cases, a lower heating rate results in a higher LSS. It is believed that a low heating rate leads to a better temperature homogeneity at the weld interface[27] which, in turn, promotes polymer flow all across the weld area. Very low heating rates would, however, lead to excessive temperature increase throughout the adherend thickness, which is undesirable as it would deform the adherends. To differentiate between the effect of the heating rate and that of the HE size, we turn our attention to welding configuration #1, which has the lowest input current of all configurations but the most conductive HE (HE A). Results show that the LSS increases compared to the other configurations done with HE A but does not reach a LSS as high as for the other HE. Therefore, the heating rate is partly responsible for the mechanical performance of the

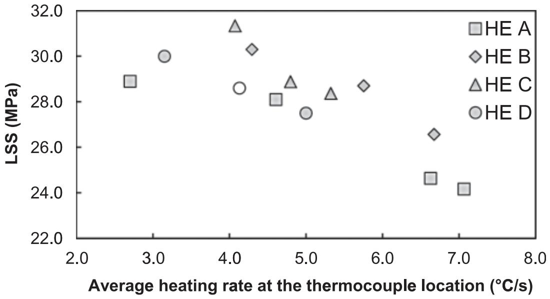

Figure 12. Lap shear strength (LSS) of induction-welded specimens as a function of the heating rate.
HE: heating element.

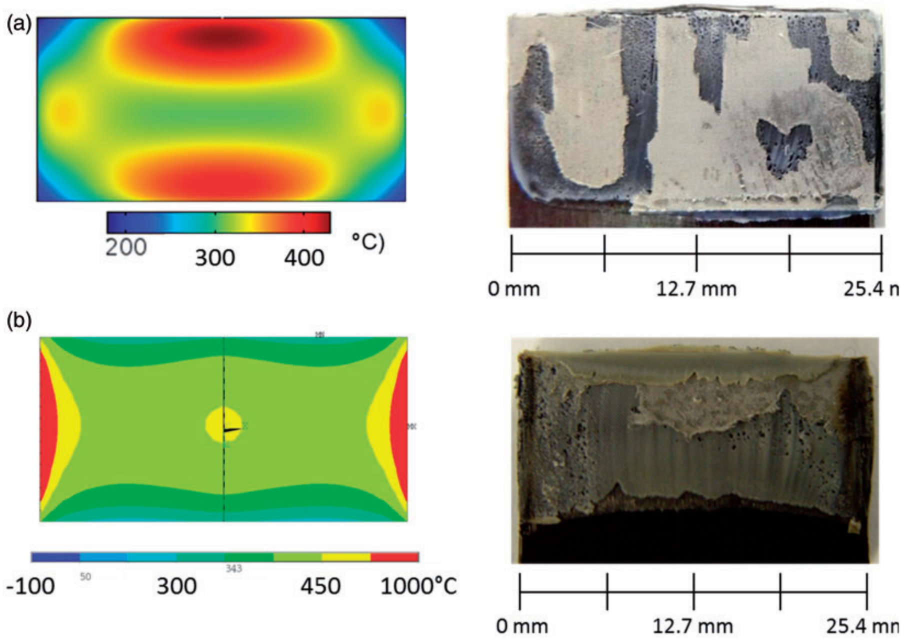

Figure 11. Thermal maps obtained by FEM and fracture surfaces of tested specimens: (a) induction-welded specimen (configuration 8, HE C, and 500 A) and (b) results of resistance-welded specimen taken from Talbot et al.[27]
FEM: finite element model; HE: heating element.

joints and other parameters, such as the HE wire diameter and open gap width, must also be taken into account to explain the variation in the joints mechanical performance.

This effect of the HE size on the LSS is depicted in Figure 13. A ratio of the fraction of open area over the wire diameter (equation (3)) is used to make a global comparison of the various HE sizes. This ratio is calculated as:

$$Ratio = \frac{heating\ element\ open\ area/total\ heating\ element\ area}{wire\ diameter} \quad (3)$$

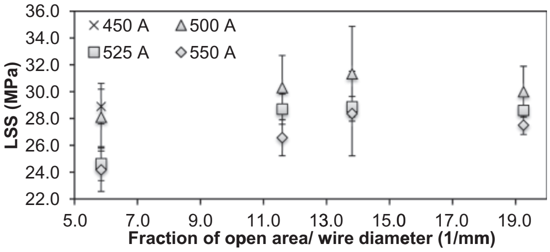

Figure 13. LSS of induction-welded specimens as a function of the HE ratio (fraction of open area/wire diameter).
LSS: lap shear strength; HE: heating element.

Increasing the open area and decreasing the wire diameter should logically improve the mechanical performance as more space is available at the weld interface for resin flow. Reducing the wire diameter (and thus the HE density, see Table 2) also means that less foreign material is present at the weld interface and that stress concentration around the wire should be reduced. Obviously, this ratio cannot be increased indefinitely as the very purpose of the HE at the interface is to generate heat. Figure 13 shows the limit of this ratio. Passed a ratio of fraction of open area over the wire diameter of around 15 to 19 mm^{-1}, the mechanical performance is no longer improved and even decreases. This result is consistent for every considered welding configuration. Studies on RW reached similar conclusions,[3] but the results obtained for the best ratio of fraction of open area over the wire diameter is shifted here as the way the heat is generated is also different (eddy currents for IW as opposed to direct input current for RW).

Failure modes analysis and cross-section micrographs

Figure 14 illustrates the cross-section micrographs of the induction-welded specimens with HE A, B, C, and D as well as the resistance-welded and ultrasonically

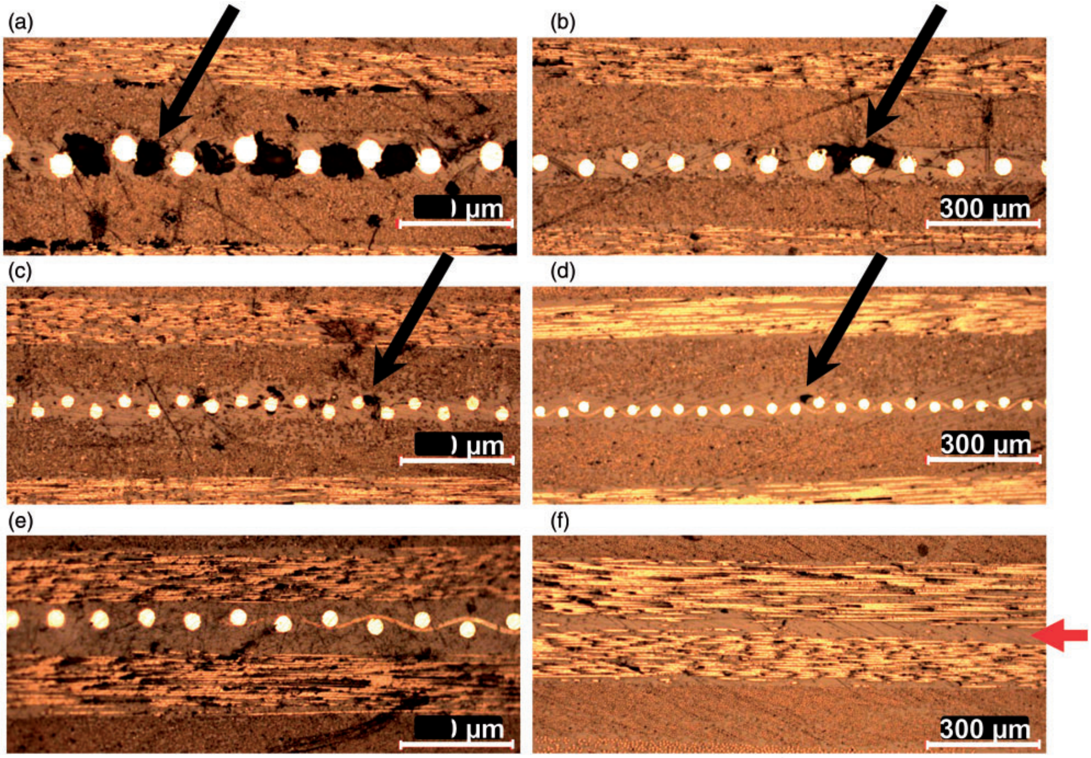

Figure 14. Cross-section micrographs of welded joints: (a) to (d) specimens welded by IW using a 500-A input current and HE A to D, respectively, (e) specimen welded by RW, and (f) specimen welded by UW. The red arrow indicates the weld line, and the black arrows indicate the voids.
HE: heating element; IW: induction welding; RW: resistance welding; UW: ultrasonic welding.

welded specimens. The first composite ply located immediately next to the weld interface appears to have the fibers perpendicular to the figure plane in a, b, c, and d and parallel to the figure plane in e and f. This is caused by the welded specimens being cut differently for microscopic observation. The actual stacking sequence of the welded specimens was the same in every case. The void content and void size in the induction-welded specimens decreases from HE A to HE D. The free volume, defined as the total open area multiplied by the HE thickness, is different for each HE, being 29 mm^3, 20 mm^3, 14 mm^3, and 11 mm^3 for HE A, B, C, and D, respectively. Therefore, the resin must flow over a larger thickness and fill a larger free volume for HE A than for HE D. In addition, for a same input power, the time the resin has to flow through the HE is shorter for HE A as it provides faster heating rates. The addition of these two factors, combined with the inherent larger size of HE A and associated stress distribution around the wires can explain the lower mechanical performances of IW configurations 2 to 4. Figure 15 illustrates the fracture surfaces of the tested specimens and provides an extra explanation for the lower mechanical performance obtained with HE A. In Figure 15(a), i.e. fracture surface of induction-welded specimen under a current of 550 A and HE A, a change of color of the PPS resin is seen. The same was observed on specimens welded using configuration #3, which corresponds to a current of 525 A and HE A. These two configurations are the ones providing the fastest heating rates (see Figure 9). They are also the ones leading to the lowest LSS. It is believed that such a high heating rate of the order of 6.6 °C/s would promote temperature non-uniformity over the weld interface, with regions of high temperature. This high temperature then causes degradation of the PPS resin. The degradation of the PPS resin along with the fast heating rates obtained with HE A also explains the higher void content seen in Figure 14(a). Reducing the welding temperature in these cases would not help in getting a better mechanical performance as non-welded regions would be created over the weld area. To avoid such a non-homogeneous temperature, the input current must be reduced or the HE must be changed for a finer one. All specimens welded under these recommended conditions experienced interlaminar failure mode, i.e. HE rupture and/or fiber damage within the adherends with associated higher LSS.

Comparison between induction, resistance, and UW

The LSS results for all welding processes are shown in Table 6. Induction-, ultrasonically-, and resistance-welded specimens presented similar mechanical performances with LSS of 31.3 MPa, 31.7 MPa, and 32.5 MPa, respectively. The results reported for the IW process are based on welding configuration 8. Overall, the LSS values are higher than what was reported previously for CF/PPS.[2] However, in Villegas et al.,[2] the material was based on a pre-impregnated carbon fiber twill weave fabric ([0/90]$_8$), instead of UD carbon fiber here ($[(0/90/\pm45)_2]_s$). Also, in Villegas et al.,[2] no HE was used for IW as the fiber architecture allowed for

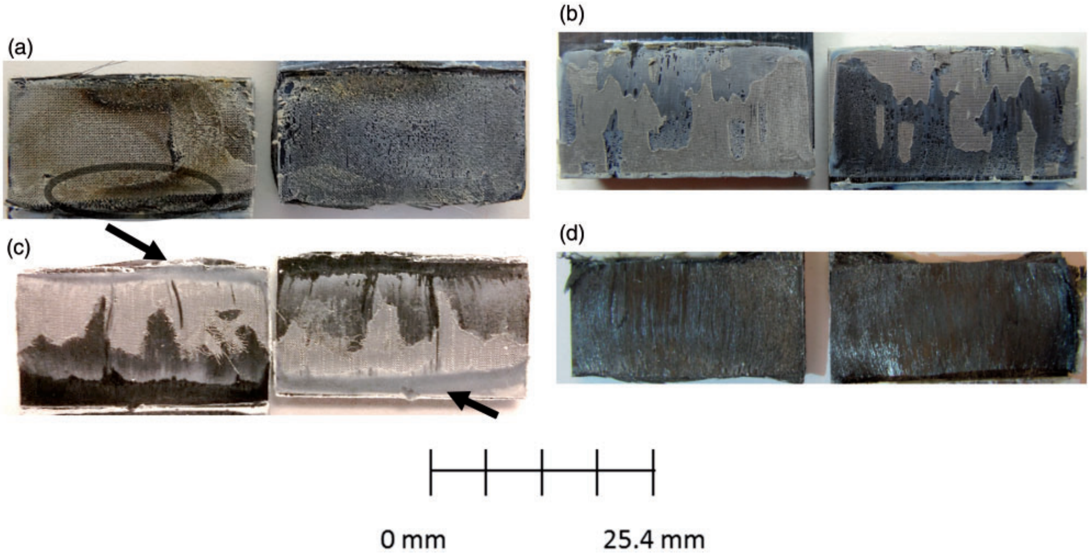

Figure 15. Fracture surfaces of welded joints: (a) specimens welded by IW with a current of 550 A and HE A, (b) specimens welded by IW with a current of 500 A and HE D, (c) specimens welded by RW, and (d) specimen welded by UW. Arrows indicate unwelded areas.
HE: heating element; IW: induction welding; RW: resistance welding; UW: ultrasonic welding.

Table 6. Comparison of LSS for joints welded by IW, RW, and UW.

Welding process	LSS (MPa)	Standard deviation (MPa)
IW (configuration #8)	31.3	3.50
RW (configuration #14)	31.7	0.95
UW (configuration #15)	32.5	1.74

LSS: lap shear strengths; IW: induction welding; RW: resistance welding; UW: ultrasonic welding.

direct heating of the adherends. The good mechanical performance obtained here shows that IW of UD CF/PPS adherends with the use of an HE represents a great alternative as an assembly process for the aerospace industry. Furthermore, in Villegas et al.,[2] the LSS of the resistance-welded specimens was reported to be 15% lower than those of the induction- or ultrasonically welded specimens. Such a decrease of the mechanical performance for the RW process is not reported here. The main reason is that the material used in Villegas et al.,[2] because of its fabric architecture, inevitability had fibers oriented parallel to the electrical current direction, therefore being more prone to causing current leakage during the welding process. The current leakage could only be avoided by drastically reducing the welding pressure to 0.1 MPa, which, in turn, significantly reduced the area effectively welded and, consequently, the LSS.[2] In the present case, however, the first ply of the UD carbon fibers adherends, i.e. the ply located immediately next to the HE, was perpendicular to the electrical current flow. This permitted the use of a higher welding pressure of 0.5 MPa without experiencing current leakage issues. Despite the higher welding pressure, visual inspection of the fracture surfaces of resistance-welded specimens (Figure 15(c)) still revealed a somewhat incomplete welded area. In effect, the resin located close to the long edges of the joint (Figure 1) was not properly melted, as indicated in Figure 15(c). As mentioned earlier, while the long edges of the joint (Figure 1) represent a cold zone in RW, they are the hottest part of the weld in IW because of the magnetic edge effect. Hotter joint long edges and therefore a potential higher weld quality in those areas did not, however, cause an increase of the LSS of the induction-welded joints as compared to the resistance-welded joints. Ultrasonically welded specimens fracture surfaces revealed some fiber deformation caused by the vibration and the resin flow at the welding interface, pushing the UD fibers in an outward direction. All welded specimens of every welding process experienced some resin and fiber squeeze out.

Overall, the study shows that similar mechanical performance can be obtained for the welded joints, no matter which of the three investigated welding processes is used. Other considerations should therefore lead the choice of a welding process for a particular application. The material and geometry of the joint are probably the considerations that should have the largest impact on the welding process selection.

Conclusion

The present study examined the IW of thermoplastic composite adherends made of UD CF/PPS plies stacked in a quasi-isotropic layup. An HE positioned at the weld interface was used to generate heating. An FEM was developed and used to predict the heating of the adherends during welding. Materials properties were identified experimentally or estimated. The importance of including the temperature dependence of the adherends properties was emphasized. A good correlation with the heating rates measured experimentally was obtained, for various HE sizes and welding parameters. The model also served to better understand the effects of the welding parameters, material properties, and HE size on the heating of the adherends. Mechanical testing results of induction-welded specimens showed that a low heating rate of 5.0 °C/s leads to good mechanical performance, when combined with a proper HE size. Comparison with RW and UW processes highlighted different heating patterns at the weld interface. Nevertheless, good joint mechanical performance can be obtained, no matter what welding process is used. The selection of a welding process for a particular application should therefore be based on other factors such as the weld geometry and size, as well as the material type.

Declaration of Conflicting Interests

The author(s) declared no potential conflicts of interest with respect to the research, authorship, and/or publication of this article.

Funding

The author(s) disclosed receipt of the following financial support for the research, authorship, and/or publication of this article: This project was funded by the Natural Sciences and Engineering Research Council of Canada (NSERC).

References

1. Van Ingen J, Buitenhuis A, Van Wijngaarden M, et al. Development of the Gulfstream G650 induction welded thermoplastic elevators and rudder. In: *SAMPE 2010 conference and exhibition "new materials and processes for a new economy,"*. Seattle, WA, USA: Society for the Advancement of Material and Process Engineering, 18 May 2010.

2. Villegas IF, Moser L, Yousefpour A, et al. Process and performance evaluation of ultrasonic, induction and resistance welding of advanced thermoplastic composites. *J Thermoplast Compos Mater* 2012; 26: 1007–1024.
3. Dubé M, Hubert P, Gallet JNAH, et al. Metal mesh heating element size effect in resistance welding of thermoplastic composites. *J Compos Mater* 2012; 46: 911–919.
4. Villegas IF. In situ monitoring of ultrasonic welding of thermoplastic composites through power and displacement data. *J Thermoplast Compos Mater* 2013; 28: 66–85.
5. Worrall C, Wise R and Kapadia A. Novel induction heating technique for joining of carbon fibre composites. In: *16th European conference on composite materials*, Sevilla, Spain, 22–26 June 2014.
6. Bayerl T, Duhovic M, Mitschang P, et al. The heating of polymer composites by electromagnetic induction – a review. *Compos Part A: Appl Sci Manuf* 2014; 57: 27–40.
7. Ahmed TJ, Stavrov D, Bersee HEN, et al. Induction welding of thermoplastic composites—an overview. *Compos Part A: Appl Sci Manuf* 2006; 37: 1638–1651.
8. Dube M, Hubert P, Yousefpour A, et al. Fatigue failure characterisation of resistance-welded thermoplastic composites skin/stringer joints. *Int J Fatigue* 2009; 31: 719–725.
9. Miller AK, Chang C, Payne A, et al. Nature of induction heating in graphite-fiber, polymer-matrix composite materials. *SAMPE J* 1990; 26: 37–54.
10. Lin W and Buneman O. Induction heating model for graphite fiber/thermoplastic matrix composites. *SAMPE J* 1991; 27: 45–51.
11. Mitschang P, Rudolf R and Neitzel M. Continuous induction welding process, modelling and realisation. *J Thermoplast Compos Mater* 2002; 15: 127–153.
12. Moser L. *Experimental analysis and modeling of susceptorless induction welding of high performance thermoplastic polymer composites*. PhD Thesis, Institute für Verbundwerkstoffe GmbH, Kaiserslautern, Germany, 2012.
13. Duhovic M, Hümbert M, Mitschang P, et al. Further advances in simulating the processing of composite materials by electromagnetic induction. In: LS-DYNA (ed.) *13th international LS-DYNA user conference*, Dearborn, Michigan, USA, 11 June 2014.
14. Duhovic M, L'Eplattenier P, Caldichoury I, et al. Advanced 3d finite element simulation of thermoplastic carbon fiber composite induction welding. In: *ECCM 16 – European conference on composite materials*, Seville, Spain, 22–26 June 2014.
15. Duhovic M, Mitschang P and Maier M. Advance in simulating the processing of composite materials by electromagnetic induction. In: LS-DYNA (ed) *9th European LS-DYNA users' conference*, Manchester, UK, 2–4 June 2013.
16. Duhovic M, Moser L, Mitschang P, et al. Simulating the joining of composite materials by electromagnetic induction. In: *12th international LS-DYNA user conference* (ed LS-DYNA), Dearborn, Michigan, USA, 3–5 June 2012.
17. Bensaid S, Trichet D and Fouladgar J. 3-D simulation of induction heating of anisotropic composite materials. *IEEE Trans Magn* 2005; 41: 1568–1571.
18. Bensaid S, Trichet D and Fouladgar J. Electromagnetic and thermal behaviors of multilayer anisotropic composite materials. *IEEE Trans Magn* 2006; 42: 995–998.
19. Wasselynck G, Trichet D and Fouladgar J. Determination of the electrical conductivity tensor of a CFRP composite using a 3-d percolation model. *IEEE Transactions on Magnetics* 2013; 49: 1825–1828.
20. Fink B, McCullough RL and Gillespie JWJ. *Induction heating of carbon-fiber composites: thermal generation model*. Aberdeen, Maryland: Army Research Laboratory, 2000.
21. Fink B, McCullough RL and Gillespie JW Jr. A local theory of heating in cross-ply carbon fiber thermoplastic composites by magnetic induction. *Polym Eng Sci* 1992; 32: 357–369.
22. Yarlagadda S, Kim HJ, Gillespie JW Jr, et al. A study on the induction heating of conductive fiber reinforced composites. *J Compos Mater* 2002; 36: 401–421.
23. Kim HJ, Yarlagadda S, Shevchenko NB, et al. Development of a numerical model to predict in-plane heat generation patterns during induction processing of carbon fiber-reinforced prepreg stacks. *J Compos Mater* 2003; 37: 1461–1483.
24. Rudolf R, Mitschang P and Neitzel M. Induction heating of continuous carbon-fibre-reinforced thermoplastics. *Compos Part A: Appl Sci Manuf* 2000; 31: 1191–1202.
25. Ruffini RS, Ruffini RT, Nemkov VS, et al. Enhancing induction heating processes by applying magnetic flux controllers. In: *Heat treating: proceedings of the 19th conference*, Cincinnati, OH, USA, 1–4 November 1999, pp.162–167. Materials Park, OH: ASM International.
26. Ageorges C, Ye L and Hou M. Experimental investigation of the resistance welding of thermoplastic-matrix composites. Part II: optimum processing window and mechanical performance. *Compos Sci Technol* 2000; 60: 1191–1202.
27. Talbot E, Hubert P, Dube M, et al. Optimization of thermoplastic composites resistance welding parameters based on transient heat transfer finite element modeling. *J Thermoplast Compos Mater* 2013; 26: 699–717.
28. Rudnev VI, Loveless D, Cook R, et al. *Handbook of induction heating*. New York: Taylor & Francis, 2002.
29. Holmes ST and Gillespie JW Jr. Thermal analysis for resistance welding of large-scale thermoplastic composite joints. *J Reinf Plast Compos* 1993; 12: 723–736.
30. Jun X and Wirtz RA. In-plane effective thermal conductivity of plain-weave screen laminates. *IEEE Trans Compon Pack Technol* 2002; 25: 615–620.
31. Ahmed TJ, Stavrov D and Bersee HEN. An experimental investigation into resistance and induction welding for aerospace structures: a comparison. In: *47th AIAA/ASME/ASCE/AHS/ASC structures, structural dynamics and materials conference*, Newport, RI, USA, 1–4 May 2006, pp.7765–7774. Reston, VA: American Institute of Aeronautics and Astronautics Inc.

32. Ho CY and Chu TK. In: CINDAS (ed.) *Electrical resistivity and thermal conductivity of nine selected aisi stainless steels*, 1977.
33. Ten Cate Advanced Composite USA Inc. TenCate Cetex® TC1100 PPS Resin System, 2013.
34. GraphiteStore. GCGW-5110, 2014.
35. Lin W. *Induction heating model for high-frequency induction joining and repair of complex-shape graphite fiber/polymer matrix composites*. Stanford: Stanford University, 1993, p. 244.
36. Fluxtrol. Ferrotron 559H: Soft magnetic composite for induction heating, 2014.